Volume 26
Number 2

December *2024*
(ISSN 1109-1606)

Journal of

APPLIED ELECTROMAGNETISM

JAE

Trans Black Sea Region Union of Applied Electromagnetism
BSUAE

Institute of Communication and Computer Systems

Athens - GREECE

Volume 26 **December 2024**
Number 2 **(ISSN 1109-1606)**

JOURNAL
OF
APPLIED ELECTROMAGNETISM

Institute of Communication and Computer Systems

Athens - GREECE

Volume 26 **Number 2**

December 2024

TRANS BLACK SEA REGION UNION OF APPLIED ELECTROMAGNETISM (BSUAE)

JOURNAL OF APPLIED ELECTROMAGNETISM

Institute of Communication and Computer Systems

Athens - GREECE

Publishing Department

Journal of Applied Electromagnetism

Copyright Form

The undersigned I confirm that I agree the publication of the article

in the Journal of Applied Electromagnetism and the copyright to belong to Trans Black Sea Union of Applied Electromagnetism. I understand that I have the full right to reuse this manuscript for my own purposes.

Name:

Surname:

Address:

E-mail:

Signed:

***Please send the previous form signed either by e-mail to pfrangos@central.ntua.gr , or by fax to the fax number: +30 210 772 2281, attention of Prof. P. Frangos.**

Address

Institute of Communication and Computer Systems,

National Technical University of Athens,

9, Iroon Polytechniou Str.,

157 73 Athens - GREECE

Tel: (+30) 210 772 3694

Fax: (+30) 210 772 2281, attention of Prof. P. Frangos

e-mail: pfrangos@central.ntua.gr

Web site: **http://jae.ece.ntua.gr**

TRANS BLACK SEA REGION UNION OF APPLIED ELECTROMAGNETISM (BSUAE)

JOURNAL OF APPLIED ELECTROMAGNETISM (JAE)

Volume 26 Number 2 December 2024

CONTENTS

In this paper an outdoor measurement campaign for almost flat terrain environment is undertaken for wireless mobile applications at frequencies 1.0 GHz and 1.5 GHz. The measured results are compared here both with the well – known in the literature "Two–Ray" (TR) model of wave propagation, as well as with the also well – known "Extended Hata" (EH) model. As a result, it is found here that under the conditions of this outdoor experiment the TR model is much more accurate, as compared to the measured results of ours. It is intended that further research by our research group will be conducted by our research group in the direction of comparison of our measured results with alternative analytical results which have been produced by us in previous publications of ours, in the "high frequency" regime.

The structures of field sources described by the wave functions of a circular cylinder have been investigated. These sources exhibit the character of two-dimensional multipoles, consisting of a set of monopoles confined within a small planar region. Multiple possible configurations have been identified for each multipole source, differing in geometric arrangement, the number of monopoles and the accuracy with which they represent the original wave field.

This paper investigates the digitization, compression and encryption of analog signals. Digitization transforms analog signals into discrete digital form, crucial for efficient data processing and transmission in diverse industries. A-law compression is used to optimize the dynamic range of the signals by reducing the data needed to represent them while maintaining acceptable quality. Results demonstrate analog-to-digital conversion of sinusoidal signal and voice using an 8-bit ADC, confirming minimal signal loss with higher quantization levels. AES encryption is used to secure the digitized and compressed signal, ensuring data privacy. Future research will explore signal recovery methods and automated encryption techniques using Simulink. This study underscores the importance of digitization and encryption technologies in advancing communication systems reliability and security.

FLAT TERRAIN MEASUREMENTS AND PATH LOSS MODELS AT 1.0 AND 1.5 GHZ

Nektarios Moraitis[*], Panayiotis Frangos[*], Ileana Popescu[*], Alexandros Rogaris[*], and Seil Sautbekov[**]

[*] School of Electrical and Computing Engineering, National Technical University of Athens, 9, Iroon Polytechniou Str., 15773 Zografou, Athens, Greece.

[**]Department of Physics and Technology, Al-Farabi Kazakh National University Almaty, Kazakhstan

E-mail: pfrangos@central.ntua.gr

(Selected from CEMA'24 Conference)

Abstract

In this paper an outdoor measurement campaign for almost flat terrain environment is undertaken for wireless mobile applications at frequencies 1.0 GHz and 1.5 GHz. The measured results are compared here both with the well – known in the literature "Two–Ray" (TR) model of wave propagation, as well as with the also well – known "Extended Hata" (EH) model. As a result, it is found here that under the conditions of this outdoor experiment the TR model is much more accurate, as compared to the measured results of ours. It is intended that further research by our research group will be conducted by our research group in the direction of comparison of our measured results with alternative analytical results which have been produced by us in previous publications of ours, in the "high frequency" regime.

1. INTRODUCTION

The problem of electromagnetic (EM) wave propagation over the flat terrain (or over a lossy medium with flat interface) is well – known in the literature as the "Sommerfeld antenna radiation problem", where the interest here is for observation points over the flat interface [1]-[23]. However, in this paper we concentrate in comparing our outdoor experimental measurements in "high frequency" regime (here for frequencies 1.0 GHz and 1.5 GHz), which are obtained here by our research group, with approximate or empirical models of electromagnetic (EM) wave propagation [24-30]. In near future proposed research by our group, we intend to compare our outdoor

experimental results measured by us here with alternative analytical results which have been produced by our research group in previous publications of ours (always in the "high frequency" regime).

This paper is organized as following: Section 2 describes the measurement equipment, as well as the procedure followed during our outdoor measurement campaign. Candidate path loss models to characterize the measured path loss are introduced and discussed in Section 3. Finally, conclusions and future research are presented in Section 4.

2. MEASUREMENT CAMPAIGN

The measurements were carried out in a football (soccer) field inside our University (NTUA) campus, in order to represent a near flat earth scenario. The field was partially covered with grass, whereas it was surrounded by tall trees. Fig. 1 illustrates the measurement environment, as well as the transmit (Tx) and receive (Rx) locations. The red circles denote the two different Tx locations, being separated about 5 m, which concurrently transmit a continuous wave (CW) signal at 1.0 GHz (Tx1), and 1.5 GHz (Tx2), respectively. It is worth noticing that under such conditions no wave interference between the two transmitted EM waves, i.e., from the two transmitting antennas, is observed, because of the fact that both transmitted waves are very narrowband, since they are CW signals.

The two (2) antennas were both mounted at a height of 2.7 m about the field surface. Two signal generators were utilized to produce the transmitted signals, which were fed, through similar 3-m low loss cables, to similar vertically polarized omnidirectional antennas. They both have a half power beamwidth (HPBW) of 45◦ in the elevation plane and a constant gain of about 0.20 dBi in the azimuth plane at the selected frequencies. The transmitted effective isotropic radiated power (e.i.r.p.), was 16.1 dBm and 18.8 dBm, at 1.0 and 1.5 GHz, respectively.

An SRM-3006 frequency selective field meter by Narda GmbH (Pfullingen, Germany) in spectrum analysis mode was employed as the receiving unit. An electric field isotropic probe was used (420 MHz - 6 GHz with a 0 dBi gain), connected to the main control unit through a 1.5-m cable. The Rx sensor was mounted on a wooden tripod at 1.7 m above the field surface. The Rx unit recorded the power samples in dBm, using a

time average of 2 minutes. The Rx sensitivity was -120 dBm. The utilized Rx equipment was calibrated according to the ISO/IEC 17025:2017 standard [24]. Table I summarizes the Tx and Rx characteristics adopted in the launched measurement campaign.

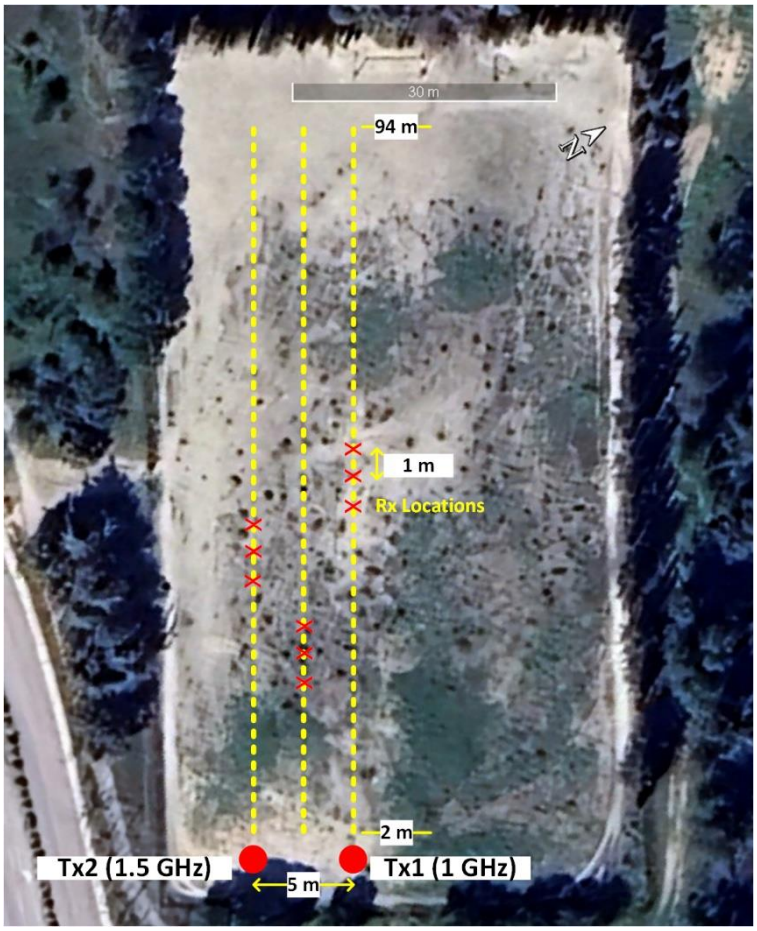

Figure 1. Measurement environment and locations.

Table 1. Transmitter and receiver characteristics during the measurement campaign at each selected frequency scenario.

	1.0 GHz	1.5 GHz
Tx power [dBm]	17	20
Tx gain [dBi]	0.20	
Cable loss [dB]	1.14	1.42
EIRP [dBm]	16.1	18.8
Rx gain [dBi]	0	
Rx sensitivity [dBm]	-120	

The Rx recorded the signal at distinct positions from 2 m up to 94 m in three (3) parallel routes, as also shown in Fig. 1, in steps of 1 m. At each measurement position the

Rx was stationary, having a line-of-sight (LOS) condition with the Tx. This entails a total number of 279 collected power samples at each frequency band.

Based on the received signal power the measured path loss PL, in decibels, at each Rx location can be described by:

$$PL = \mathrm{P}_{\mathrm{Tx}} - L_{\mathrm{c}} + G_{\mathrm{Tx}} + G_{\mathrm{Rx}} - P_r \tag{1}$$

where P_{Tx} denotes the Tx power in dBm, L_{c} indicates the cable losses, G_{Tx}, G_{Rx} stands for the Tx and Rx gains, respectively, in dBi, and P_r is the received signal power in dBm. Therefore, from (1), 279 path loss samples are resolved at each examined frequency scenario at a specific distance d_D, in meters, between Tx and Rx (length of the direct ray) that is given by:

$$d_D = \sqrt{d^2 + (h_t - h_r)^2} \tag{2}$$

where d indicates the horizontal (ground) distance, in meters, between Tx and Rx, and h_t, h_r designate the Tx and Rx heights (2.7 and 1.7 m), respectively.

The raw data for both scenarios are shown in Fig. 2, where the received power versus distance is depicted. It should be pointed out that the distance from Tx in logarithmic scale, in meters, represents the direct distance (d_D) between Tx and Rx.

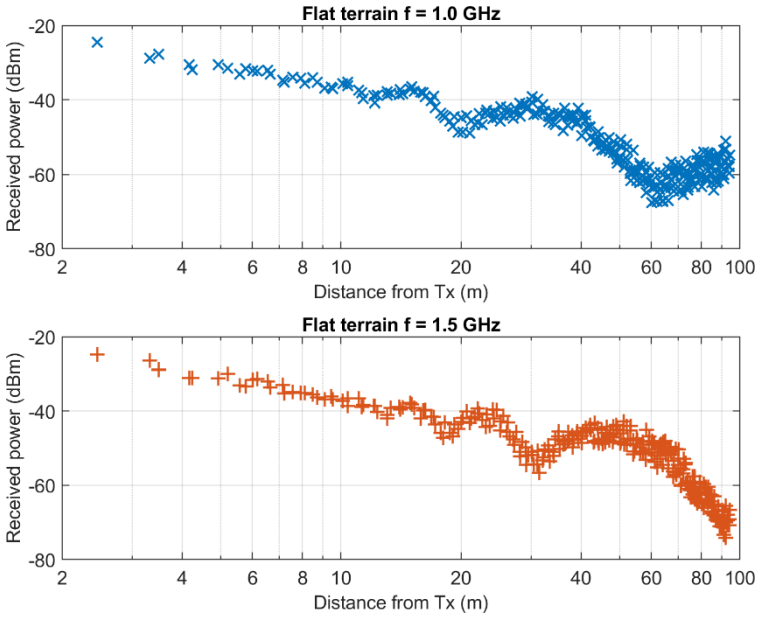

Figure 2. Received signal power at each measured location at 1 and 1.5 GHz.

Clearly the power samples imply a flat terrain pattern, where power drops are encountered at specific distances. This resembles to a two-ray pattern model, which will be examined for its appropriateness to model the measured path loss in Section 3, below, along with appropriate Extended Hata model, as well, for comparison purposes.

3. PATH LOSS MODELS RESULTS AND DISCUSSION

The two-ray model describes the signal propagation using two components. The direct ray between Tx and Rx and a ground reflected path ray. The path loss, in decibels, based on the two-ray model is given by [25]:

$$PL = 20\log_{10}\left(\frac{4\pi d}{\lambda}\right) - 20\log_{10}\left|1+\Gamma_{\mathrm{V}}\, \mathrm{e}^{j\Delta\varphi}\right| \tag{3}$$

where λ is the wavelength, in meters, at each selected frequency, and d is the ground (horizontal) distance between Tx and Rx, as previously mentioned. Furthermore, Γ_{V} denotes the vertical polarization reflection coefficient of the ground reflected path, and $\Delta\varphi$ stands for the phase difference between the direct and the ground paths. The reflection coefficient is described by:

$$\Gamma_{\mathrm{V}} = \frac{-\varepsilon_r \sin\theta_i + \sqrt{\varepsilon_r - (\cos\theta_i)^2}}{\varepsilon_r \sin\theta_i + \sqrt{\varepsilon_r - (\cos\theta_i)^2}} \tag{4}$$

where θ_i, is the *"grazing angle"* of the incident wave (i.e., the angle between the incident EM wave and the flat terrain), and ε_r is the relative permittivity of the ground. Assuming a very dry ground, ε_r = 3 according to [26]. Furthermore, the grazing angle in (4), is related to the geometrical propagation characteristics according to:

$$\begin{aligned} \sin\theta_i &= \left(\frac{h_t + h_r}{d_G}\right) \\ \cos\theta_i &= \left(\frac{d}{d_G}\right) \end{aligned} \tag{5}$$

where d_G denotes the length of the ground reflected ray, in meters, which can be calculated by:

$$d_G = \sqrt{d^2 + (h_t + h_r)^2} \tag{6}$$

Finally, the phase difference between of the path lengths between the direct and the ground reflected rays are given by:

$$\Delta\varphi = \frac{2\pi}{\lambda}(d_D - d_G) \tag{7}$$

where d_D and d_G are provided by (2) and (6), respectively.

Apart from the two-ray path loss model, the measured path loss is also compared with the *"Extended Hata"* model [27]. A rural/open area environment is assumed in this case; therefore, the path loss is given by:

$$PL = PL_U - 4.78(\log_{10}[\min\{\max\{150, f\}, 2000\}])^2 + 18.33\log_{10}[\min\{\max\{150, f\}, 2000\}] - 40.94 \tag{8}$$

where f is the operating frequency in MHz, and PL_U the path loss considering the urban environment. The latter parameter can be calculated according to:

$$\begin{aligned} PL_U &= 46.3 + 33.9\log_{10}(2000) + 10\log_{10}(f/2000) - 13.82\log_{10}(\max\{30, h_t\}) \\ &\quad + (44.9 - 6.55\log_{10}(\max\{30, h_t\}))\log_{10}(d_D) - a(h_r) - b(h_t) \end{aligned} \tag{9}$$

where d_D is the direct ray distance, converted in kilometres, between Tx and Rx, and f the operating frequency in MHz. Further, $a(h_r)$ and $b(h_t)$, are the correction factors for the Rx and Tx, respectively, taking into account their specific heights h_r and h_t in meters. The correction factors are adopted for the rural/open area locations and can be calculated by:

$$b(h_t) = \min\{0, 20\log_{10}(h_t/30)\} \tag{10}$$

and

$$a(h_r) = (1.1\log_{10}(f) - 0.7)\min\{10, h_r\} - (1.56\log_{10}(f) - 0.8) + \max\{0, 20\log_{10}(h_r/10)\} \tag{11}$$

This model is widely used and is applicable for frequencies up to 3 GHz, and distances up to 40 km, respectively.

The results are presented in Fig. 3 where the path loss versus distance (in logarithmic scale) is provided along with the two different empirical models for comparison.

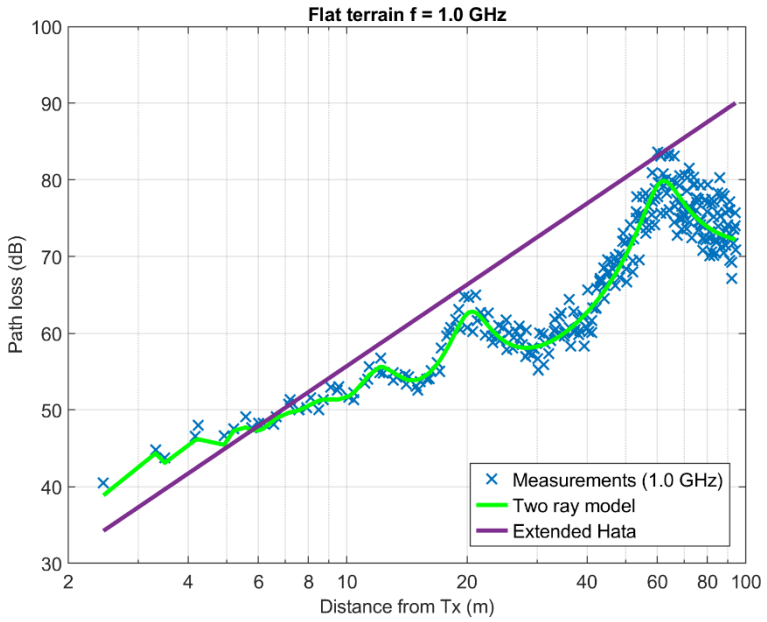

(a)

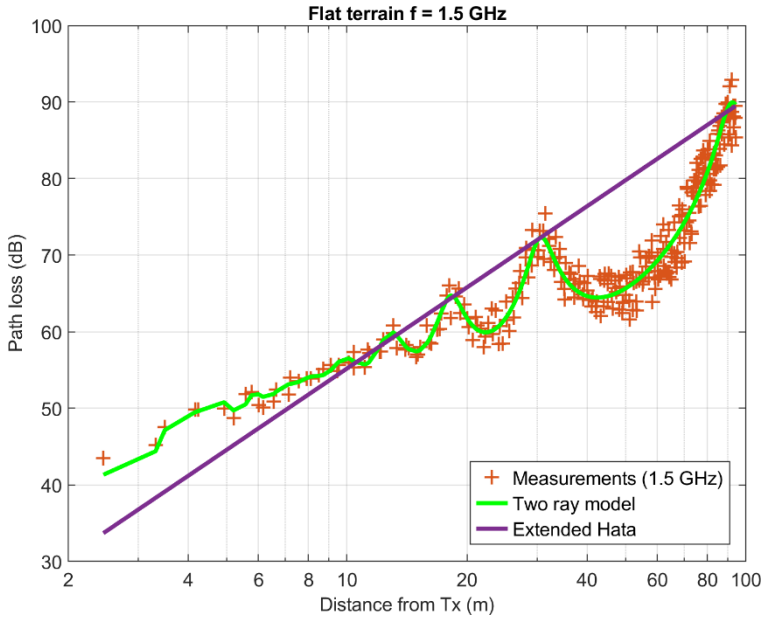

(b)

Figure 3. Path loss results versus distance. (a) 1.0 GHz. and (b) 1.5 GHz.

It is evident that "two-ray model" adapts better to the measured path loss, as it takes into account the geometrical characteristics of the propagating signal in the specific flat-terrain environment. On the other hand, the "Extended Hata model", predicts well the path loss in the first few meters (about 10 m for 1.0 GHz measurements, or about 15 m, for 1.0 GHz measurements), but diverges afterwards compared to the measured samples.

To compare quantitatively and validate the realized outcome, appropriate error metrics are applied, in order to analyze the statistical error of each model [28], [29]. The mean absolute error (MAE), in decibels, is given by:

$$\mathrm{MAE} = \frac{1}{N}\sum_{i=1}^{N}\left|PL_i^{meas} - PL_i^{pred}\right| \tag{12}$$

where PL_i^{meas} and PL_i^{meas} stand for the measured and predicted path loss values, respectively, and i is the index of the measured sample. Finally, N is the total number of path loss samples (279 at each frequency scenario). The mean absolute percentage error (MAPE) is calculated according to:

$$\mathrm{MAPE} = \frac{1}{N}\sum_{i=1}^{N}\left|\frac{PL_i^{meas} - PL_i^{pred}}{PL_i^{meas}}\right| \times 100\% \tag{13}$$

Finally, the root mean square error (RMSE), which actually represents the shadow factor is given, in decibels, by:

$$\mathrm{RMSE} = \sqrt{\frac{1}{N}\sum_{i=1}^{N}\left(PL_i^{meas} - PL_i^{pred}\right)^2} \tag{14}$$

The prediction errors are computed in the following applying (12)-(14), for each assessed path loss model. An acceptable RMSE for a path loss model is 6-7 dB for urban locations, and higher than 10 up to 15 dB, for suburban and rural/open areas [30].

Table II summarizes the numerical results of the obtained error metrics for each model and frequency scenario.

Table 2. Statistical results between measured and predicted path loss for Two-Ray (TR) and Extended Hata (EH) models at each frequency scenario.

Model	**Metric**	**1.0 GHz**	**1.5 GHz**
TR	MAE [dB]	1.8	1.7
	MAPE [%]	2.6	2.4
	RMSE [dB]	2.3	2.1
EH	MAE [dB]	9.6	7.6
	MAPE [%]	14.4	11.3
	RMSE [dB]	10.8	9.1

The results in Table II reveal that "Two-Ray" (TR) model is better applicable in a near flat-terrain environment, that is much lower errors are obtained, as compared with the "Extended Hata" (EH) model. In terms of RMS error, TR model adjusts slightly

better at 1.0 GHz, nevertheless the error values between the two frequency scenarios are comparable. On the other hand, despite the high errors, EH model adapts better at 1.5 GHz, which implies that is more suitable at higher frequency applications over flat-terrain. However, at 1.0 GHz the results are discouraging, delivering an RMS error of 10.8 dB, which is higher that the acceptable value of 10 dB for rural/open areas, as suggested in [30].

Therefore, based on the above analysis, EH empirical model is not recommended for accurate path loss predictions in flat-terrain scenarios. Instead, geometrical optics (GO) models, such as “TR model”, are better applicable, providing accurate path loss predictions, thus being recommendable for such flat-terrain applications.

4. CONCLUSION

In this paper we presented an outdoor experimental measurement campaign of our research group from propagation of EM waves over flat terrain (at 1.0 GHz and 1.5 GHz) and compared the experimental results with the “two-ray” model, as well as with the “Extended Hata” propagation model. It was found that the former model (“two-ray” propagation model) provides very good accuracy to the measured data (as this might be expected in the “high frequency regime”, examined here).

As future work, the authors intend to assess additional path loss models of theirs (obtained by them through their previous research experience on EM propagation problems over the terrain), and validate their suitability to predict accurately the path loss in near flat-terrain scenarios.

ACKNOWLEDGMENT

The authors would like to thank the Kazakhstan Ministry of Education and Research for a research grant with title "AP19676900, The new technique for evaluation of the propagation of radio waves for terrestrial communications", which supported this research. In addition, they would like to thank Ph.D. candidate Mr. Basil Massinas (at NTUA) for his valuable help in the preparation of this paper.

REFERENCES

[1] A. N. Sommerfeld, "Propagation of waves in wireless telegraphy," *Ann. Phys.*, 1909, 28, pp. 665-737.

[2] K. A. Norton, "The propagation of radio waves over the surface of the earth and in the upper atmosphere," *Proc. Inst. Radio Eng.*, vol. 24, no. 10, pp. 1367-1387, Oct. 1935. doi:10.1109/JRPROC.1936.227360.

[3] A. K. Norton, "The propagation of radio waves over the surface of the earth and in the upper atmosphere," *Proc. Inst. Radio Eng.*, vol. 25, no. 9, pp. 1203-1236, Sep. 1937. doi:10.1109/JRPROC.1937.228544.

[4] J. Wait, "Launching a surface wave over the earth," *Electron. Lett.*, vol. 3, no. 9, pp. 396-397, Sep. 1967. doi:10.1049/el:19670307.

[5] R. J. King, "Electromagnetic wave propagation over a constant impedance plane," *Radio Sci.*, vol. 4, no. 3, pp. 255-268, Mar. 1969. doi:10.1029/RS004i003p00255.

[6] T. K. Sarkar, W. Dyab, M. N. Abdallah, M. Salazar-Palma, M. V. S. N. Prasad, S. W. Ting, and S. Barbin, "Electromagnetic macro modeling of propagation in mobile wireless communication: Theory and experiment," *IEEE Antennas Propag. Mag.*, 2012, 54, pp. 17-43, doi:10.1109/MAP.2012.6387779.

[7] J. G. V. Bladel, The Sommerfeld Dipole Problem. In Electromagnetic Fields, J. Wiley and Sons, Inc.: Hoboken, NJ, USA, 2007; Section 9.3, pp. 448–452.

[8] G. Tyras, Field of a Dipole in a Stratified Medium. In Radiation and Propagation of Electromagnetic Waves; Academic Press, Inc., New York, NY, USA, 1969; Section 6, pp. 133–160.

[9] Y. Rahmat-Samii, R. Mittra, P. Parhami, "Evaluation of Sommerfeld integrals for lossy half-space problems," *Electromagnetics*, vol. 1, no. 1, pp. 1-28, 1981. doi:10.1080/02726348108915122.

[10] R. E. Collin, "Hertzian dipole radiating over a lossy earth or sea: some early and late 20th-century controversies," *IEEE Antennas Propag. Mag.*, 2004, vol. 46, no. 2, pp. 64-79, Apr. 2004. doi:10.1109/MAP.2004.1305535.

[11] K. A. Michalski, "On the efficient evaluation of integral arising in the Sommerfeld halfspace problem," *IEE Proc.-Microwaves, Antennas Propag.*, 1985, 132, pp. 312–318, doi:10.1049/ip-h-2.1985.0056.

[12] G. Pelosi, J. L. Volakis, "On the centennial of Sommerfeld's solution to the problem of dipole radiation over an imperfectly conducting half space," *IEEE Antennas Propag. Mag.*, 2010, 52, pp. 198-201, doi:10.1109/MAP.2010.5586629.

[13] J. R. Wait, "The ancient and modern history of EM ground-wave propagation," *IEEE Antennas Propag. Mag.*, 1998, 40, pp. 7-24, doi:10.1109/74.735961.

[14] A. Baños, *Dipole Radiation in the Presence of a Conducting Half-Space*, Pergamon Press, Oxford, UK, 1966; pp. 151–158.

[15] S. S. Sautbekov, R.N. Kasimkhanova, and P. V. Frangos, "Modified solution of Sommerfelds's problem," in Proc. CEMA'10 Conference, Athens, Greece, 7–9 October 2010; pp. 5-8. Available online: http://rcvt.tu-sofia.bg/CEMA/proceedings/CEMA_2010_proc.pdf (accessed on May 2021).

[16] S. Sautbekov, "The generalized solutions of a system of Maxwell's equations for the uniaxial anisotropic media," in Electromagnetic Waves Propagation in Complex Matter"; IntechOpen Limited: London, UK, 2011; Chapter 1, pp. 1–24, doi:10.5772/16886.

[17] K. Ioannidi, C. Christakis, S. Sautbekov, P. Frangos, and S. K. Atanov, "The radiation problem from a vertical Hertzian dipole antenna above flat and lossy ground: Novel formulation in the spectral domain with closed-form analytical solution in the high frequency regime," *Int. J. Antennas Propag. (IJAP)*, 2014, Special Issue on 'Propagation of Electromagnetic Waves in Terrestrial Environment for Applications in Wireless Telecommunications', doi:10.1155/2014/989348.

[18] S. Bourgiotis, K. Ioannidi, C. Christakis, S. Sautbekov, P. Frangos, "The radiation problem from a vertical short dipole antenna above flat and lossy ground: Novel formulation in the spectral domain with numerical solution and closed-form analytical solution in the high frequency regime," in Proc. CEMA'14 Conference, Sofia, Bulgaria, 16–18 October 2014; pp. 12–18, Available online: http://rcvt.tu-sofia.bg/CEMA/proceedings/CEMA_2014_proc.pdf (accessed on May 2021).

[19] S. Bourgiotis, A. Chrysostomou, K. Ioannidi; S. Sautbekov, and P. Frangos, "Radiation of a vertical dipole over flat and lossy ground using the spectral domain approach: Comparison of stationary phase method analytical solution with numerical integration results," Electronics and Electrical Engineering Journal, 2015, 21, pp. 38-41, doi:10.5755/j01.eee.21.3.10268.

[20] A. Chrysostomou, S. Bourgiotis, S. Sautbekov, K. Ioannidi, and P. Frangos, "Radiation of a vertical dipole antenna over flat and lossy ground: Accurate electromagnetic field calculation using the spectral domain approach along with redefined integral representations and corresponding novel analytical solution," Electronics and Electrical Engineering Journal, 2016, 22, pp. 54–61, doi:10.5755/j01.eie.22.2.14592.

[21] S. Sautbekov, S. Bourgiotis, A. Chrysostomou, and P. Frangos, "A novel asymptotic solution to the Sommerfeld radiation problem: Analytic field expressions and the emergence of the surface waves," PIER M, 2018, 64, pp. 9–22, doi:10.2528/PIERM17082806.

[22] S. Bourgiotis, P. Frangos, S. Sautbekov and M. Pshikov, "The Evaluation of an asymptotic solution to the Sommerfeld radiation problem using an efficient method for the calculation of Sommerfeld integrals in the spectral domain," 'Electronics Journal, MDPI Publisher, 1, https://doi.org/10.3390/electronics1010000, https://www.mdpi.com/journal/electronics, Special Issue on 'Propagation of Electromagnetic Waves in Terrestrial Environment for Applications in Wireless Telecommunications and Radar Systems', June 2021.

[23] J. Fikioris, I*ntroduction to Antenna Theory and Propagation of Electromagnetic Waves*. National Technical University of Athens: Athens, Greece, 1982. (In Greek).

[24] International Organization for Standardization, "General requirements for the competence of testing and calibration laboratories," ISO/IEC 17025:2017, Geneva, Switzerland, Nov. 2017.

[25] T. S. Rappaport, *Wireless Communications: Principles and Practice*. (2nd ed.), Prentice Hall, Upper Saddle River, New Jersey, 2002.

[26] Electrical Characteristics of the Surface of the Earth, document ITU-R P.527-6, International Telecommunication Union, Geneva, Switzerland, Sep. 2021.

[27] Monte Carlo simulation methodology for the use in sharing and compatibility studies between different radio services or systems, document ITU-R SM.2028-2, International Telecommunication Union, Geneva, Switzerland, Jun. 2017.
[28] E. Östlin, H. J. Zepernick, and H. Suzuki, "Macrocell path-loss prediction using artificial neural networks," *IEEE Trans. Veh. Technol.*, vol. 59, no. 6, pp. 2735-2747, Jul. 2010.
[29] Y. Zhang, et al., "Path loss prediction based on machine learning: Principle, method, and data expansion," *Appl. Sci.*, vol. 9, no. 9, pp. 1-18, May 2019.
[30] J. D. Parsons, *The Mobile Radio Propagation Channel*. 2nd ed., New York: Wiley, 2000.

STUDY OF FIELD SOURCE STRUCTURES DESCRIBED BY CIRCULAR CYLINDER WAVE FUNCTIONS

Ivane Darsavelidze[*, **]

[*] Ivane Javakhishvili Tbilisi State University, 0179 Tbilisi, Georgia

[**] LEPL Institute "Optica", 0179 Tbilisi, Georgia

E-mail: ivane.darsavelidze@tsu.ge

Abstract

The structures of field sources described by the wave functions of a circular cylinder have been investigated. These sources exhibit the character of two-dimensional multipoles, consisting of a set of monopoles confined within a small planar region. Multiple possible configurations have been identified for each multipole source, differing in geometric arrangement, the number of monopoles and the accuracy with which they represent the original wave field.

1. INTRODUCTION

The work focuses on investigating the structures of sources of fields which are described by the wave functions of a circular cylinder [1]

$$H_n^{(1)}(k\rho)\cos(n\varphi),\ H_n^{(1)}(k\rho)\sin(n\varphi). \tag{1}$$

Here k is a wave number, (ρ, φ) are the polar coordinates of the observation point, $H_n^{(1)}(k\rho)$ is a Hankel function and n is a non-negative integer. As it is known, the functions (1) are the solutions of the two dimensional Helmholtz equation. They are used for studying the problems, related to the harmonic in time wave processes, when the area is bounded by the circular cylinder surface. It is supposed, that the time factor is $e^{-i\omega t}$.

The corresponding zero-order function $H_0^{(1)}(k\rho)$ describes the field of the elementary two dimensional source (monopole), which is propagating as a travelling cylindrical wave, from the origin. Since the expression of this field depends only on the coordinate ρ, then its amplitude radiation pattern will have the shape of a circle. The situation changes for the fields (1) at subsequent values of n. Since they also depend on

the angular coordinate φ, then their radiation patterns have more complicated shape (Figure 1), which indicates the multipole nature of the sources of such fields. The objective is to analyze the structures of these sources.

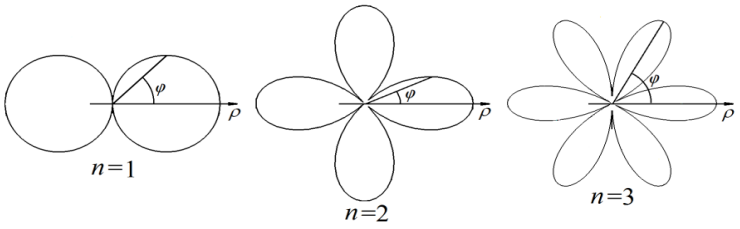

Figure 1. Examples of radiation patterns for $H_n^{(1)}(k\rho)\cos(n\varphi)$

This paper proposes two main approaches to solving the problem. The first one is based on the consideration the amplitude radiation patterns of fields (1) and the construction the linear differential operators. Their effect on the $H_0^{(1)}(k\rho)$ yields to the original fields [2]. The second one is based on the application of the known addition theorem for the Bessel cylindrical functions. As a result of investigation, four types of multipoles were identified. They differ by the geometric construction, number of monopoles and also by the accuracy of the original field's representation.

2. PROBLEM STATEMENT

Let us focus on the radiation patterns of the fields (1), at initial values of n =1,2,3,…(Figure 2).

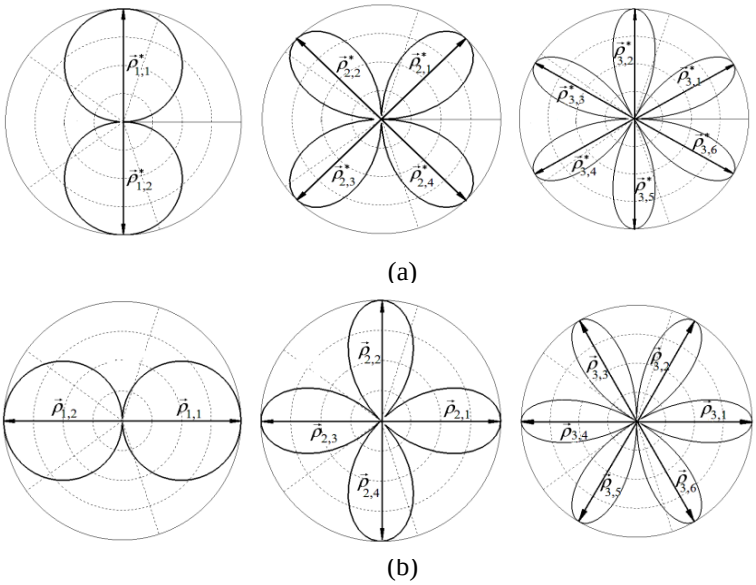

Figure 2. Examplesof radiation patterns: (a) $H_n^{(1)}(k\rho)\cos(n\varphi)$ and (b) $H_n^{(1)}(k\rho)\sin(n\varphi)$

It can be seen, that each of them consist of $2n$ lobes, the directions of which can be determined by the unit vectors

$$\vec{\rho}_{n,j}=\left\{\cos\varphi_{n,j},\sin\varphi_{n,j}\right\},\ \vec{\rho}^{\,*}_{n,j}=\left\{\cos\varphi^{*}_{n,j},\sin\varphi^{*}_{n,j}\right\}, \tag{2}$$

Where

$$\varphi_{n,j}=\frac{\pi}{n}\left(j-1\right),\ \varphi^{*}_{n,j}=\frac{\pi}{n}\left(j-\frac{1}{2}\right),\ j=1,...,2n. \tag{3}$$

2. 1. First Kind Operators

Let consider the linear differential operators with the form

$$\hat{L}_n=\frac{\left(-1\right)^n 2^{n-1}}{nk^n}\sum_{j=1}^{n}\left(-1\right)^{j+1}\frac{\partial^n}{\partial\vec{\rho}_{n,j}{}^n},\ \hat{L}^{*}_n=\frac{\left(-1\right)^n 2^{n-1}}{nk^n}\sum_{j=1}^{n}\left(-1\right)^{j+1}\frac{\partial^n}{\partial\vec{\rho}^{\,*}_{n,j}{}^n}. \tag{4}$$

Here, under the summation sign, there are derivative operators of n-th order along the directions of the vectors (2), i.e.

$$\frac{\partial^n}{\partial\vec{\rho}_{n,j}{}^n}=\left(\cos\varphi_{n,j}\frac{\partial}{\partial x}+\sin\varphi_{n,j}\frac{\partial}{\partial y}\right)^n,\ \frac{\partial^n}{\partial\vec{\rho}^{\,*}_{n,j}{}^n}=\left(\cos\varphi^{*}_{n,j}\frac{\partial}{\partial x}+\sin\varphi^{*}_{n,j}\frac{\partial}{\partial y}\right)^n.$$

Applying Newton's binomial formula and introducing the notation

$$B_{n,q}=\sum_{j=1}^{n}\left(-1\right)^{j+1}\left(\cos\varphi_{n,j}\right)^{n-q}\left(\sin\varphi_{n,j}\right)^{q},\ B^{*}_{n,q}=\sum_{j=1}^{n}\left(-1\right)^{j+1}\left(\cos\varphi^{*}_{n,j}\right)^{n-q}\left(\sin\varphi^{*}_{n,j}\right)^{q},$$

operators (4) can be represented as

$$\hat{L}_n=\frac{\left(-1\right)^n 2^{n-1}}{nk^n}\sum_{q=0}^{n}C_n^q B_{n,q}\frac{\partial^n}{\partial x^{n-q}\partial y^q},\ \hat{L}^{*}_n=\frac{\left(-1\right)^n 2^{n-1}}{nk^n}\sum_{q=0}^{n}C_n^q B^{*}_{n,q}\frac{\partial^n}{\partial x^{n-q}\partial y^q}.$$

Calculating the $B_{n,q}$ and $B^{*}_{n,q}$ coefficients, for the different values of n, it can be noted that they can be determined as

$$B_{n,q}=\left(-1\right)^{\lfloor q/2\rfloor}\left[1+\left(-1\right)^q\right]\left(n/2^n\right),\ B^{*}_{n,q}=\left(-1\right)^{\lfloor q/2\rfloor}\left[1-\left(-1\right)^q\right]\left(n/2^n\right),$$

where $\lfloor q/2\rfloor$ is the integer part of the number $q/2$. Then, taking into account that in the expressions of the operators $\hat{L}_n$ and $\hat{L}^{*}_n$ the terms only with even and odd values of q respectively must remain, then finally, we obtain

$$\hat{L}_n=\frac{\left(-1\right)^n}{k^n}\sum_{\alpha=0}^{\lfloor n/2\rfloor}\left(-1\right)^{\alpha}C_n^{2\alpha}\frac{\partial^n}{\partial x^{n-2\alpha}\partial y^{2\alpha}},\ \hat{L}^{*}_n=\frac{\left(-1\right)^n}{k^n}\sum_{\beta=1}^{\lfloor (n+1)/2\rfloor}\left(-1\right)^{\beta+1}C_n^{2\beta-1}\frac{\partial^n}{\partial x^{n-2\beta+1}\partial y^{2\beta-1}}. \tag{5}$$

Let us now consider a homogeneous polynomial of degree n, from variables x, y,

$$f_n(x,y)=\sum_{\alpha=0}^{n}A_{n,\alpha}x^{n-\alpha}y^{\alpha},$$

where $A_{n,\alpha}$ are the known coefficients. We will say that the linear differential operator $\hat{F}_n$ is the eigen-operator for this polynomial, if it is the result of the following transformation:

$$x\to-\frac{1}{k}\frac{\partial}{\partial x},\ y\to-\frac{1}{k}\frac{\partial}{\partial y}.$$

So, it will have the form

$$\hat{F}_n=\frac{(-1)^n}{k^n}\sum_{\alpha=0}^{n}A_{n,\alpha}\frac{\partial^n}{\partial x^{n-\alpha}\partial y^{\alpha}}. \tag{6}$$

Let us show, that $\hat{L}_n$ and $\hat{L}_n^*$ are the eigen-operators for the cylindrical harmonics $\rho^n\cos(n\varphi)$ and $\rho^n\sin(n\varphi)$ [3]. For this, we will use well-known expression for the power of a complex number:

$$\rho^n e^{\pm in\varphi}=(x\pm iy)^n=\sum_{\alpha=0}^{\lfloor n/2\rfloor}(-1)^{\alpha}C_n^{2\alpha}x^{n-2\alpha}y^{2\alpha}\pm i\sum_{\beta=1}^{\lfloor (n+1)/2\rfloor}(-1)^{\beta+1}C_n^{2\beta-1}x^{n-2\beta+1}y^{2\beta-1},$$

from where follows the next homogeneous polynomials

$$\rho^n\cos(n\varphi)=\sum_{\alpha=0}^{\lfloor n/2\rfloor}(-1)^{\alpha}C_n^{2\alpha}x^{n-2\alpha}y^{2\alpha},\ \rho^n\sin(n\varphi)=\sum_{\beta=1}^{\lfloor (n+1)/2\rfloor}(-1)^{\beta+1}C_n^{2\beta-1}x^{n-2\beta+1}y^{2\beta-1}.$$

The eigen-operators of these polynomials, according to the definition (6) will coincide with $\hat{L}_n$ and $\hat{L}_n^*$. For the eigen-operator of polynomial $(x\pm iy)^n$ we have the expression

$$\frac{(-1)^n}{k^n}\left(\frac{\partial}{\partial x}\pm i\frac{\partial}{\partial y}\right)^n=\hat{L}_n\pm i\hat{L}_n^*. \tag{7}$$

The operators $\hat{L}_n$ and $\hat{L}_n^*$ give ability to connect the original *n*-order fields (1) with the zero-order field $H_0^{(1)}(k\rho)$. Namely, we will show that for any $n\geq 1$,

$$\hat{L}_nH_0^{(1)}(k\rho)=H_n^{(1)}(k\rho)\cos(n\varphi),\ \hat{L}_n^*H_0^{(1)}(k\rho)=H_n^{(1)}(k\rho)\sin(n\varphi). \tag{8}$$

For this, we combine functions (1) as

$$S_n^{\pm}(\rho,\varphi)=H_n^{(1)}(w)e^{\pm in\varphi}, \tag{9}$$

where $w = k\rho$ and consider the partial derivatives of function $S_n^{\pm}(\rho,\varphi)$ by *x* and *y*. After some transformations we will have

$$\frac{1}{k}\frac{\partial S_n^{\pm}(\rho,\varphi)}{\partial x} = \left[\frac{dH_n^{(1)}(w)}{dw}\cos\varphi \mp i\frac{n}{w}H_n^{(1)}(w)\sin\varphi\right]e^{\pm in\varphi},$$

$$\frac{1}{k}\frac{\partial S_n^{\pm}(\rho,\varphi)}{\partial y} = \left[\frac{dH_n^{(1)}(w)}{dw}\sin\varphi \pm i\frac{n}{w}H_n^{(1)}(w)\cos\varphi\right]e^{\pm in\varphi},$$

from where we can write

$$\frac{1}{k}\frac{\partial S_n^{\pm}(\rho,\varphi)}{\partial x} \pm i\frac{1}{k}\frac{\partial S_n^{\pm}(\rho,\varphi)}{\partial y} = \left[\frac{dH_n^{(1)}(w)}{dw} - \frac{n}{w}H_n^{(1)}(w)\right]e^{\pm i(n+1)\varphi},$$

or taking into account known recurrent formula [4]

$$\frac{dH_n^{(1)}(w)}{dw} - \frac{n}{w}H_n^{(1)}(w) = -H_{n+1}^{(1)}(w), \tag{10}$$

we finally obtain:

$$-\frac{1}{k}\left(\frac{\partial}{\partial x} \pm i\frac{\partial}{\partial y}\right)S_n^{\pm}(\rho,\varphi) = S_{n+1}^{\pm}(\rho,\varphi). \tag{11}$$

As a special case, when *n* =0, we have

$$-\frac{1}{k}\left(\frac{\partial}{\partial x} \pm i\frac{\partial}{\partial y}\right)S_0^{\pm}(\rho,\varphi) = S_1^{\pm}(\rho,\varphi).$$

Similarly, when *n* =1,

$$-\frac{1}{k}\left(\frac{\partial}{\partial x} \pm i\frac{\partial}{\partial y}\right)S_1^{\pm}(\rho,\varphi) = S_2^{\pm}(\rho,\varphi),$$

or

$$\frac{(-1)^2}{k^2}\left(\frac{\partial}{\partial x} \pm i\frac{\partial}{\partial y}\right)^2 S_0^{\pm}(\rho,\varphi) = S_2^{\pm}(\rho,\varphi).$$

If we continue this process, in general we can write

$$\frac{(-1)^n}{k^n}\left(\frac{\partial}{\partial x} \pm i\frac{\partial}{\partial y}\right)^n S_0^{\pm}(\rho,\varphi) = S_n^{\pm}(\rho,\varphi),$$

or considering that $S_0^{\pm}(\rho,\varphi) = H_0^{(1)}(w)$, using (7) and (9),

$$\left(\hat{L}_n \pm i\hat{L}_n^*\right)H_0^{(1)}(k\rho) = H_n^{(1)}(k\rho)e^{\pm in\varphi}.$$

The last expression is equivalent to two expressions

$$\hat{L}_n H_0^{(1)}(k\rho) + i\hat{L}_n^* H_0^{(1)}(k\rho) = H_n^{(1)}(k\rho)\cos(n\varphi) + iH_n^{(1)}(k\rho)\sin(n\varphi),$$

$$\hat{L}_n H_0^{(1)}(k\rho) - i\hat{L}_n^* H_0^{(1)}(k\rho) = H_n^{(1)}(k\rho)\cos(n\varphi) - iH_n^{(1)}(k\rho)\sin(n\varphi),$$

from which equalities (8) follow. In expanded form we can write

$$\frac{(-1)^n 2^{n-1}}{nk^n}\sum_{j=1}^{n}(-1)^{j+1}\frac{\partial^n H_0^{(1)}(k\rho)}{\partial\vec{\rho}_{n,j}{}^n} = H_n^{(1)}(k\rho)\cos(n\varphi), \tag{12}$$

$$\frac{(-1)^n 2^{n-1}}{nk^n}\sum_{j=1}^{n}(-1)^{j+1}\frac{\partial^n H_0^{(1)}(k\rho)}{\partial\vec{\rho}_{n,j}^{*\,n}} = H_n^{(1)}(k\rho)\sin(n\varphi). \tag{13}$$

2. 2. Second Kind Operators

Let us now consider operators of the form

$$\hat{M}_n = \frac{2^{n-2}(n-1)!}{(k\rho_0)^n}\sum_{j=1}^{2n}(-1)^{j+1}\sum_{m=0}^{n}\frac{(-1)^m\rho_0{}^m}{m!}\frac{\partial^m}{\partial\vec{\rho}_{n,j}{}^m}, \tag{14}$$

$$\hat{M}_n^* = \frac{2^{n-2}(n-1)!}{(k\rho_0)^n}\sum_{j=1}^{2n}(-1)^{j+1}\sum_{m=0}^{n}\frac{(-1)^m\rho_0{}^m}{m!}\frac{\partial^m}{\partial\vec{\rho}_{n,j}^{*\,m}}, \tag{15}$$

where ρ_0 is some coefficient. Applying Newton's binomial formula, after a series of transformations, these operators can be written as

$$\hat{M}_n = \frac{2^{n-1}(n-1)!}{(k\rho_0)^n}\sum_{m=0}^{n}\frac{\rho_0{}^m}{m!}\sum_{q=0}^{m}C_m^q B_{n,m,q}\frac{\partial^m}{\partial x^{m-q}\partial y^q},\ \hat{M}_n^* = \frac{2^{n-1}(n-1)!}{(k\rho_0)^n}\sum_{m=0}^{n}\frac{\rho_0{}^m}{m!}\sum_{q=0}^{m}C_m^q B_{n,m,q}^*\frac{\partial^m}{\partial x^{m-q}\partial y^q},$$

where the following notations are introduced

$$B_{n,m,q} = \frac{1}{2}\left[(-1)^m + (-1)^n\right]\sum_{j=1}^{n}(-1)^{j+1}\left(\cos\varphi_{n,j}\right)^{m-q}\left(\sin\varphi_{n,j}\right)^q,$$

$$B_{n,m,q}^* = \frac{1}{2}\left[(-1)^m + (-1)^n\right]\sum_{j=1}^{n}(-1)^{j+1}\left(\cos\varphi_{n,j}^*\right)^{m-q}\left(\sin\varphi_{n,j}^*\right)^q.$$

Calculating the values of the coefficients $B_{n,m,q}$ and $B_{n,m,q}^*$ for different *n*, we can notice that

$$B_{n,m,q} = (-1)^n\delta_{mn}B_{n,q},\ B_{n,m,q}^* = (-1)^n\delta_{mn}B_{n,q}^*,$$

where δ_{mn} is Kronecker delta. As a result, the operators $\hat{M}_n$ and $\hat{M}_n^*$ will be transformed to the form

$$\hat{M}_n = \frac{(-1)^n 2^{n-1}}{nk^n} \sum_{q=0}^{n} C_n^q B_{n,q} \frac{\partial^n}{\partial x^{n-q} \partial y^q}, \; \hat{M}_n^* = \frac{(-1)^n 2^{n-1}}{nk^n} \sum_{q=0}^{n} C_n^q B_{n,q}^* \frac{\partial^n}{\partial x^{n-q} \partial y^q},$$

i.e. they coincide with the first type operators $\hat{L}_n$ and $\hat{L}_n^*$. Thus, similarly to expressions (12) and (13), we write

$$\frac{2^{n-2}(n-1)!}{(k\rho_0)^n} \sum_{j=1}^{2n} (-1)^{j+1} \sum_{m=0}^{n} \frac{(-1)^m \rho_0^{\,m}}{m!} \frac{\partial^m H_0^{(1)}(k\rho)}{\partial \vec{\rho}_{n,j}^{\,m}} = H_n^{(1)}(k\rho)\cos(n\varphi), \tag{16}$$

$$\frac{2^{n-2}(n-1)!}{(k\rho_0)^n} \sum_{j=1}^{2n} (-1)^{j+1} \sum_{m=0}^{n} \frac{(-1)^m \rho_0^{\,m}}{m!} \frac{\partial^m H_0^{(1)}(k\rho)}{\partial \vec{\rho}_{n,j}^{\,*\,m}} = H_n^{(1)}(k\rho)\sin(n\varphi). \tag{17}$$

3. FIRST TYPE CIRCULAR MULTIPOLE

Let us first consider expressions (12) and (13). Let us replace the directional derivatives in them by the corresponding central finite differences [5]. If the difference step is denoted by ρ_0, then for the outer area ($\rho > (n/2)\rho_0$) we will have the approximate equalities

$$\frac{2^{n-1}}{n(k\rho_0)^n} \sum_{j=1}^{n} \sum_{m=0}^{n} (-1)^{m+n+j+1} C_n^m H_0^{(1)}\left(k \left| \vec{\rho} - \left(m - \frac{n}{2} \right) \rho_0 \vec{\rho}_{n,j} \right| \right) \approx H_n^{(1)}(k\rho)\cos(n\varphi), \tag{18}$$

$$\frac{2^{n-1}}{n(k\rho_0)^n} \sum_{j=1}^{n} \sum_{m=0}^{n} (-1)^{m+n+j+1} C_n^m H_0^{(1)}\left(k \left| \vec{\rho} - \left(m - \frac{n}{2} \right) \rho_0 \vec{\rho}_{n,j}^{\,*} \right| \right) \approx H_n^{(1)}(k\rho)\sin(n\varphi), \tag{19}$$

where $\vec{\rho}$ is the radius vector of the observation point, with coordinates (ρ, φ).The left parts of these expressions describe the multipole field, the monopoles of which are located in points with radius vectors $(m - n/2)\rho_0 \vec{\rho}_{n,j}$ or $(m - n/2)\rho_0 \vec{\rho}_{n,j}^{\,*}$ respectively and have the amplitudes $\left(2^{n-1}/n\right)(k\rho_0)^{-n}(-1)^{m+n+j+1} C_n^m$. The radius of a given multipole is determined as $(n/2)\rho_0$, i.e. for the fixed value of ρ_0, increases with increasing n. The total number of the monopoles depends on the parity of n. For odd n, it is $n(n+1)$. For even n, some monopoles end up in the center, which corresponds to one monopole 1of total amplitude. The total number of monopoles, in this case, is n^2+1. The structure of the resulting multipole, which we will call the first type circular multipole, is shown on the Figure 3. As we see, the monopoles are located on concentric circles, along the lobes of the corresponding field pattern.

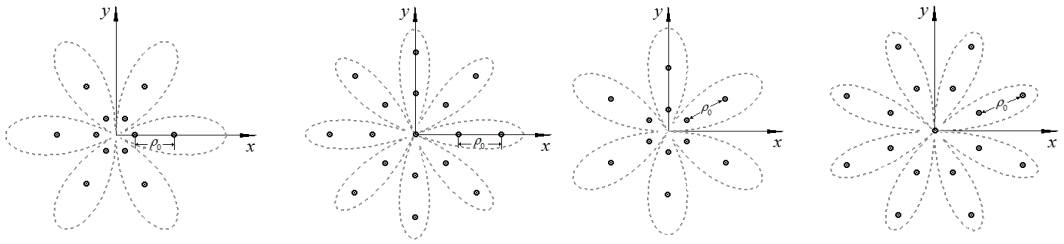

Figure 3. The first type of circular multipole, which describes the field: (a) $H_n^{(1)}(k\rho)\cos(n\varphi)$and (b) $H_n^{(1)}(k\rho)\sin(n\varphi)$, when n=3 and n=4

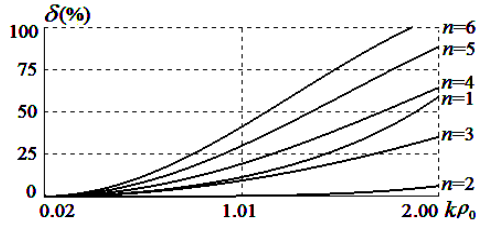

Figure 4. The dependence of the error on the value of $k\rho_0$

To determine the accuracy of the representation of fields (1) by this multipole, the dependence of the average relative error [6] of expressions (18) and (19) on the value $k\rho_0$, has been studied. These expressions have the same errors, therefore, for definiteness, only expression (18) is considered. Graphs of the resulting error for the initial values of n, are shown on Figure 4. Despite the fact that the error for n = 1 is greater than for n = 2 and n = 3, it gradually increases with increasing n. In addition, the size of the multipole also increases.

Thus, fields (1) can be approximately described by the first type circular multipole. At the same time, to ensure the same accuracy as n increases, the value of ρ_0 (determining the size of the multipole) should be reduced.

4. SECOND TYPE CIRCULAR MULTIPOLE

The other multipole type can be obtained from the expressions (16) and (17), if we notice that the inner sums of their left parts represent the first n+1 terms of the Taylor series of functions $H_0^{(1)}\left(k\left|\vec{\rho}-\rho_0\vec{\rho}_{n,j}\right|\right)$ and $H_0^{(1)}\left(k\left|\vec{\rho}-\rho_0\vec{\rho}^{\,*}_{n,j}\right|\right)$. After appropriate substitution, for the area $\rho > \rho_0$, approximately we will have

$$\frac{2^{n-2}(n-1)!}{(k\rho_0)^n}\sum_{j=1}^{2n}(-1)^{j+1}H_0^{(1)}\left(k\left|\vec{\rho}-\rho_0\vec{\rho}_{n,j}\right|\right)\approx H_n^{(1)}(k\rho)\cos(n\varphi), \qquad (20)$$

$$\frac{2^{n-2}(n-1)!}{(k\rho_0)^n}\sum_{j=1}^{2n}(-1)^{j+1}H_0^{(1)}\left(k\left|\vec{\rho}-\rho_0\vec{\rho}_{n,j}^{*}\right|\right)\approx H_n^{(1)}(k\rho)\sin(n\varphi). \quad (21)$$

Analyzing these approximate equalities, we come to the conclusion that $2n$ monopoles, with radius vectors $\rho_0\vec{\rho}_{n,j}$ and $\rho_0\vec{\rho}_{n,j}^{*}$, radiate the total field of the form $H_n^{(1)}(k\rho)\cos(n\varphi)$ and $H_n^{(1)}(k\rho)\sin(n\varphi)$ respectively. These monopoles are located on a circle with a radius ρ_0 and their amplitudes are $2^{n-2}(n-1)!(k\rho_0)^{-n}(-1)^{j+1}$. The multiplier $(-1)^{j+1}$ shows that each subsequent monopole oscillates in the opposite phase to the previous one.

The structure of the multipole that emerges, referred to as the second type circular multipole, is illustrated in Figure 5. It can be seen that the number of monopoles coincides with the number of original field pattern lobes.

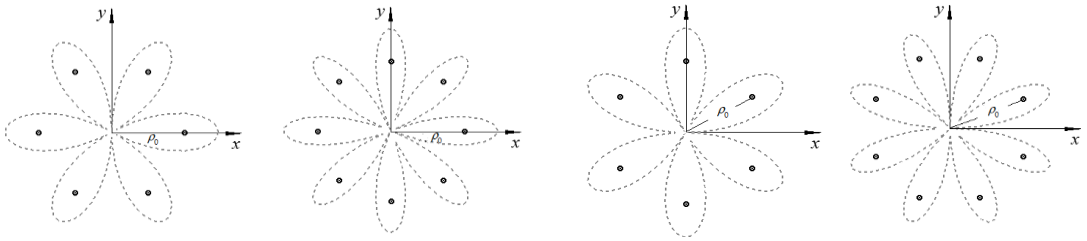

Figure 5. The second type of circular multipole, which describes the field: (a) $H_n^{(1)}(k\rho)\cos(n\varphi)$ and (b) $H_n^{(1)}(k\rho)\sin(n\varphi)$, when n=3and n=4

Figure 6 presents the dependence of the average relative error of expression (20) on the value $k\rho_0$, for several initial values of n. It can be seen that the greatest error is observed in case when n = 1, and for subsequent values of n, unlike the previous case (Figure 4), the error, on the contrary, decreases. So, starting from n = 3, in the given scales of the figure, the corresponding error graphs actually essentially merge with the horizontal axis. This indicates that the second type multipole represents the original fields with greater accuracy. Moreover, the number of monopoles reduces, making it more efficient than the first type multipole.

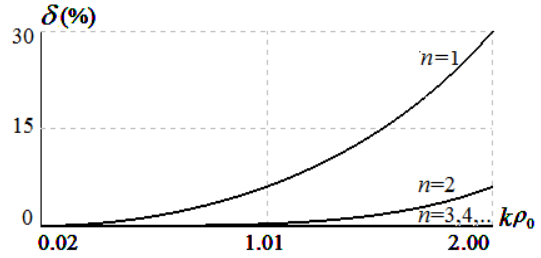

Figure 6. The dependence of the error on the value of $k\rho_0$

5. APPLICATION OF THE ADDITION THEOREM

Let us present the mathematical expression of the well-known addition theorem [1, 8] for cylindrical functions,

$$H_0^{(1)}\left(k\left|\vec{\rho}-\vec{\rho}_0\right|\right)=J_0\left(k\rho_0\right)H_0^{(1)}\left(k\rho\right)+2\sum_{m=1}^{\infty}J_m\left(k\rho_0\right)H_m^{(1)}\left(k\rho\right)\cos\left[m\left(\varphi-\varphi_0\right)\right]. \qquad (22)$$

Here $\vec{\rho}_0$ is a radius vector of point with coordinates (ρ_0, φ_0), located on a circle l_0, radius ρ_0 and centered at the origin. It is assumed that the observation point (ρ, φ) is located in outer area ($\rho > \rho_0$). In outer area the considered row converges uniformly. Next, two more types of multipoles, that describe the fields (1) are obtained, based on the application of expression (22).

5.1. Third Type of Circular Multipole

Let's multiply both sides of (22) by $\cos\left(n\varphi_0\right)$ ($\sin\left(n\varphi_0\right)$) and integrate along the circle l_0. After a series of calculations, we obtain the expressions

$$\left[2\pi\rho_0 J_n\left(k\rho_0\right)\right]^{-1}\int_{l_0}H_0^{(1)}\left(k\left|\vec{\rho}-\vec{\rho}_0\right|\right)\cos\left(n\varphi_0\right)dl_0=H_n^{(1)}\left(k\rho\right)\cos\left(n\varphi\right), \qquad (23)$$

$$\left[2\pi\rho_0 J_n\left(k\rho_0\right)\right]^{-1}\int_{l_0}H_0^{(1)}\left(k\left|\vec{\rho}-\vec{\rho}_0\right|\right)\sin\left(n\varphi_0\right)dl_0=H_n^{(1)}\left(k\rho\right)\sin\left(n\varphi\right). \qquad (24)$$

Let us replace the integrals in (23) and (24) with the corresponding integral sums. If N is a sufficiently large number, then as a result we obtain approximate equalities

$$\left[NJ_n\left(k\rho_0\right)\right]^{-1}\sum_{j=1}^{N}H_0^{(1)}\left(k\left|\vec{\rho}-\rho_0\vec{\rho}_{N,j}\right|\right)\cos\left(n\varphi_{N,j}\right)\approx H_n^{(1)}\left(k\rho\right)\cos\left(n\varphi\right), \qquad (25)$$

$$\left[NJ_n\left(k\rho_0\right)\right]^{-1}\sum_{j=1}^{N}H_0^{(1)}\left(k\left|\vec{\rho}-\rho_0\vec{\rho}^{\,*}_{N,j}\right|\right)\sin\left(n\varphi^{*}_{N,j}\right)\approx H_n^{(1)}\left(k\rho\right)\sin\left(n\varphi\right), \qquad (26)$$

where

$$\vec{\rho}_{N,j}=\left\{\cos\varphi_{N,j},\sin\varphi_{N,j}\right\},\ \vec{\rho}^{\,*}_{N,j}=\left\{\cos\varphi^{*}_{N,j},\sin\varphi^{*}_{N,j}\right\},$$

$$\varphi_{N,j}=\frac{2\pi}{N}\left(j-1\right),\ \varphi^{*}_{N,j}=\frac{2\pi}{N}\left(j-\frac{1}{2}\right),\ j=1,...,N\ .$$

Consequently, a set of N monopoles on a circle of radius ρ_0, having amplitudes $\left[NJ_n\left(k\rho_0\right)\right]^{-1}$, emit a total field of type (1) in the outer region ($\rho>\rho_0$). The difference between the resulting third type of multipole and the second is the number N of its monopoles, which in this case is not limited. It's interesting to compare their accuracy.

For this purpose, let us denote the left and right parts of expressions (25) and (26), respectively, as $L^{III}_{N,n}\left(\vec{\rho}\right)$, $R_n\left(\vec{\rho}\right)$ and $L^{III*}_{N,n}\left(\vec{\rho}\right)$, $R^{*}_n\left(\vec{\rho}\right)$. Then we can briefly write

$$L^{III}_{N,n}\left(\vec{\rho}\right)\approx R_n\left(\vec{\rho}\right),\ L^{III*}_{N,n}\left(\vec{\rho}\right)\approx R^{*}_n\left(\vec{\rho}\right).$$

Let's consider a special case when N= 2n. Note that then

$$\varphi_{N,j}=\varphi_{n,j},\ \varphi^{*}_{N,j}=\varphi^{*}_{n,j},\ \vec{\rho}_{N,j}=\vec{\rho}_{n,j},\ \vec{\rho}^{\,*}_{N,j}=\vec{\rho}^{\,*}_{n,j},\ \cos\left(n\varphi_{N,j}\right)=\sin\left(n\varphi^{*}_{N,j}\right)=\left(-1\right)^{j+1}.$$

In addition, if we assume that the value of $k\rho_0$ (the perimeter of the multipole in units of wavelength) is so small that inequality $0<k\rho_0\le\sqrt{n+1}$ holds, then we can use the well-known asymptotic expression [7]

$$J_n\left(k\rho_0\right)\approx\frac{1}{n!}\left(\frac{k\rho_0}{2}\right)^n.$$

As a result, the left sides $L^{III}_{N,n}\left(\vec{\rho}\right)$ and $L^{III*}_{N,n}\left(\vec{\rho}\right)$, for N= 2n, will be transformed to the form

$$L^{III}_{N,n}\left(\vec{\rho}\right)\Big|_{N=2n}=\frac{2^{n-1}\left(n-1\right)!}{\left(k\rho_0\right)^n}\sum_{j=1}^{2n}\left(-1\right)^{j+1}H_0^{(1)}\left(k\left|\vec{\rho}-\rho_0\vec{\rho}_{n,j}\right|\right),$$

$$L^{III*}_{N,n}\left(\vec{\rho}\right)\Big|_{N=2n}=\frac{2^{n-1}\left(n-1\right)!}{\left(k\rho_0\right)^n}\sum_{j=1}^{N}\left(-1\right)^{j+1}H_0^{(1)}\left(k\left|\vec{\rho}-\rho_0\vec{\rho}^{\,*}_{n,j}\right|\right).$$

Comparing them with the left sides $L^{II}_n\left(\vec{\rho}\right)$ and $L^{II*}_n\left(\vec{\rho}\right)$ of expressions (20) and (21) we notice that

$$L^{III}_{N,n}\left(\vec{\rho}\right)\Big|_{N=2n}=2L^{II}_n\left(\vec{\rho}\right),\ L^{III*}_{N,n}\left(\vec{\rho}\right)\Big|_{N=2n}=2L^{II*}_n\left(\vec{\rho}\right).$$

But on the other hand, according to (20) and (21), we have

$$L^{II}_n\left(\vec{\rho}\right)\approx R_n\left(\vec{\rho}\right),\ L^{II*}_n\left(\vec{\rho}\right)\approx R^{*}_n\left(\vec{\rho}\right),$$

from which

$$L^{III}_{N,n}(\vec{\rho})\big|_{N=2n} \approx 2R_n(\vec{\rho}),\ L^{III*}_{N,n}(\vec{\rho})\big|_{N=2n} \approx 2R^*_n(\vec{\rho}).$$

Thus, for N= 2n, approximate equalities (25) and (26) are violated. For the relative error at the considered point of the plane, we will have

$$\delta(\vec{\rho}) = \frac{L^{III}_{N,n}(\vec{\rho})\big|_{N=2n} - R_n(\vec{\rho})}{R_n(\vec{\rho})}100\% \approx \frac{2R_n(\vec{\rho}) - R_n(\vec{\rho})}{R_n(\vec{\rho})}100\% = 100\%,$$

$$\delta^*(\vec{\rho}) = \frac{L^{III*}_{N,n}(\vec{\rho})\big|_{N=2n} - R^*_n(\vec{\rho})}{R^*_n(\vec{\rho})}100\% \approx \frac{2R^*_n(\vec{\rho}) - R^*_n(\vec{\rho})}{R^*_n(\vec{\rho})}100\% = 100\%.$$

Consequently, to ensure sufficient accuracy of the representation of fields (1) by this type of circular multipole, the number N of its monopoles must satisfy condition $N > 2n$. This makes it non-optimal, in comparison with the circular multipole of the second type.

5.2. The Linear Multipole

Let us consider the addition theorem (22) again. Through numerical calculations one can be convinced that if the value of $k\rho_0$ satisfies the condition

$$k\rho_0 \le n/4, \tag{27}$$

then with sufficient accuracy we can limit ourselves to the first n terms of the series. Let us assume thatφ_0= 0 and condition (27) is satisfied. Then we can write

$$H^{(1)}_0\left(k\left|\vec{\rho} - \vec{\rho}_0\right|\right) \approx J_0(k\rho_0)H^{(1)}_0(k\rho) + 2\sum_{m=1}^{n} J_m(k\rho_0)H^{(1)}_m(k\rho)\cos(m\varphi),\ (\rho > \rho_0). \tag{28}$$

Let us now consider n+1 points on the abscissa axis, with radius vectors

$$\vec{\rho}_{n,\alpha} = \left\{(\alpha - n/2)d_n, 0, 0\right\},\ \alpha = 0,...,n \tag{29}$$

Notice, that if n is odd number, then for the given points, the condition $\left|\vec{\rho}_{n,\alpha}\right| \ne 0$, $\alpha = 0,...,n$ will take a place. If n is even number, then $\left|\vec{\rho}_{n,n/2}\right| = 0$. We choose the distance d_n between neighboring points in such a way that kd_n= 1/2. In this case, for all values of the vectors $\vec{\rho}_{n,\alpha}$, the inequality $k\left|\vec{\rho}_{n,\alpha}\right| \le n/4$ will take place. Let's say n is an odd number. Then, by virtue of (27) and (28), we write

$$H^{(1)}_0\left(k\left|\vec{\rho} - \vec{\rho}_{n,\alpha}\right|\right) \approx J_0\left(k\left|\vec{\rho}_{n,\alpha}\right|\right)H^{(1)}_0(k\rho) + 2\sum_{m=1}^{n} J_m\left(k\left|\vec{\rho}_{n,\alpha}\right|\right)H^{(1)}_m(k\rho)\cos\left(m\varphi_{n,\alpha}\right),$$

where $\varphi_{n,\alpha}$ is an angle between $\vec{\rho}_{n,\alpha}$ and $\vec{\rho}$ vectors. If *n* is an even number, then the angle $\varphi_{n,\alpha}$ loses its meaning at $\alpha = n/2$. Therefore, in this case we write

$$H_0^{(1)}\left(k\left|\vec{\rho}-\vec{\rho}_{n,\alpha}\right|\right)\Big|_{\alpha\neq n/2} \approx J_0\left(k\left|\vec{\rho}_{n,\alpha}\right|\right)\Big|_{\alpha\neq n/2} H_0^{(1)}\left(k\rho\right)+2\sum_{m=1}^{n} J_m\left(k\left|\vec{\rho}_{n,\alpha}\right|\right)\cos\left(m\varphi_{n,\alpha}\right)\Big|_{\alpha\neq n/2} H_m^{(1)}\left(k\rho\right),$$

$$H_0^{(1)}\left(k\left|\vec{\rho}-\vec{\rho}_{n,\alpha}\right|\right)\Big|_{\alpha=n/2} = H_0^{(1)}\left(k\rho\right).$$

Let's introduce unknown quantities $A_{n,\alpha}$ and compose a sum of the form

$$\sum_{\alpha=0}^{n}(-1)^{\alpha} A_{n,\alpha} H_0^{(1)}\left(k\left|\vec{\rho}-\vec{\rho}_{n,\alpha}\right|\right). \tag{30}$$

Based on the previous expressions, we can write

$$\sum_{\alpha=0}^{n}(-1)^{\alpha} A_{n,\alpha} H_0^{(1)}\left(k\left|\vec{\rho}-\vec{\rho}_{n,\alpha}\right|\right) \approx S_{0,n} H_0^{(1)}\left(k\rho\right)+2\sum_{m=1}^{n} S_{m,n} H_m^{(1)}\left(k\rho\right)\cos\left(m\varphi\right). \tag{31}$$

The quantities $S_{0,n}$ and $S_{m,n}$, for odd *n*, are determined as

$$S_{0,n}=\sum_{\alpha=0}^{n}(-1)^{\alpha} A_{n,\alpha} J_0\left(k\left|\vec{\rho}_{n,\alpha}\right|\right),\ S_{m,n}=\sum_{\alpha=0}^{n}(-1)^{\alpha} A_{n,\alpha} J_m\left(k\left|\vec{\rho}_{n,\alpha}\right|\right)\cos\left(m\varphi_{n,\alpha}\right).$$

For even *n*, we respectively have

$$S_{0,n}=(-1)^{n/2} A_{n,n/2}+\sum_{\substack{\alpha=0\\ \alpha\neq n/2}}^{n}(-1)^{\alpha} A_{n,\alpha} J_0\left(k\left|\vec{\rho}_{n,\alpha}\right|\right),\ S_{m,n}=\sum_{\substack{\alpha=0\\ \alpha\neq n/2}}^{n}(-1)^{\alpha} A_{n,\alpha} J_m\left(k\left|\vec{\rho}_{n,\alpha}\right|\right)\cos\left(m\varphi_{n,\alpha}\right).$$

Taking into account the obvious equalities

$$\left|\vec{\rho}_{n,\alpha}\right|=\left|\vec{\rho}_{n,n-\alpha}\right|,\ \cos\left(m\varphi_{n,n-\alpha}\right)=\cos\left(m\varphi\right),\ \cos\left(m\varphi_{n,\alpha}\right)=\cos\left[m\left(\pi-\varphi\right)\right]=(-1)^m\cos\left(m\varphi\right),$$

expressions for $S_{0,n}$ and $S_{m,n}$ can be written in a more convenient form. So, for odd *n*,

$$S_{0,n}=\sum_{\alpha=0}^{(n-1)/2}(-1)^{\alpha}\left(A_{n,\alpha}-A_{n,n-\alpha}\right)J_0\left(k\left|\vec{\rho}_{n,\alpha}\right|\right),$$

$$S_{m,n}=\sum_{\alpha=0}^{(n-1)/2}(-1)^{\alpha}\left[(-1)^m A_{n,\alpha}-A_{n,n-\alpha}\right]J_m\left(k\left|\vec{\rho}_{n,\alpha}\right|\right)$$

and for even *n*, respectively

$$S_{0,n}=(-1)^{n/2} A_{n,n/2}+\sum_{\alpha=0}^{(n/2)-1}(-1)^{\alpha}\left(A_{n,\alpha}+A_{n,n-\alpha}\right)J_0\left(k\left|\vec{\rho}_{n,\alpha}\right|\right),$$

$$S_{m,n}=\sum_{\alpha=0}^{(n/2)-1}(-1)^{\alpha}\left[(-1)^m A_{n,\alpha}+A_{n,n-\alpha}\right]J_m\left(k\left|\vec{\rho}_{n,\alpha}\right|\right).$$

We now require that the quantities $S_{0,n}$ and $S_{m,n}$ satisfy the conditions

$$S_{0,n}=0,\ S_{m,n}=\frac{1}{2}\delta_{mn}. \tag{32}$$

In this case, from expression (31), taking into account (29), we obviously obtain

$$\sum_{\alpha=0}^{n}(-1)^{\alpha}A_{n,\alpha}H_0^{(1)}\left(k\left|\vec{\rho}-\left(\alpha-\frac{n}{2}\right)d_n\vec{x}\right|\right)\approx H_n^{(1)}(k\rho)\cos(n\varphi). \tag{33}$$

Note that if we consider $n+1$ points on the ordinate axis, with radius vectors

$$\vec{\rho}^{\,*}_{n,\alpha}=\{0,(\alpha-n/2)d_n,0\},\ \alpha=0,...,n, \tag{34}$$

then, similarly to (33), we obtain

$$\sum_{\alpha=0}^{n}(-1)^{\alpha}A_{n,\alpha}H_0^{(1)}\left(k\left|\vec{\rho}-\left(\alpha-\frac{n}{2}\right)d_n\vec{y}\right|\right)\approx H_n^{(1)}(k\rho)\sin(n\varphi). \tag{35}$$

Thus, the problem is reduced to determining the coefficients $A_{n,\alpha}$, for which we use conditions (32). These conditions, in expanded form, taking into account the expressions for $S_{0,n}$ and $S_{m,n}$, will be written for odd n as

$$\sum_{\alpha=0}^{(n-1)/2}(-1)^{\alpha}\left[(-1)^m A_{n,\alpha}-A_{n,n-\alpha}\right]J_m\left(k\left|\vec{\rho}_{n,\alpha}\right|\right)=\frac{1}{2}\delta_{mn},\ m=0,...,n,$$

and for even n, respectively as

$$\begin{cases}(-1)^{n/2}A_{n,n/2}+\sum\limits_{\alpha=0}^{(n/2)-1}(-1)^{\alpha}\left(A_{n,\alpha}+A_{n,n-\alpha}\right)J_0\left(k\left|\vec{\rho}_{n,\alpha}\right|\right)=0\\ \sum\limits_{\alpha=0}^{(n/2)-1}(-1)^{\alpha}\left[(-1)^m A_{n,\alpha}+A_{n,n-\alpha}\right]J_m\left(k\left|\vec{\rho}_{n,\alpha}\right|\right)=\frac{1}{2}\delta_{m,n}\end{cases},\ m=1,...,n.$$

These expressions represent a system of linear algebraic equations with respect to unknown coefficients $A_{n,\alpha}$. The number of equations, as well as unknowns, is $n+1$. Note that through a series of transformations of these systems, this number can be reduced. Thus, for odd n, the first $(n+1)/2$ unknowns can be found by solving the system

$$\sum_{\alpha=0}^{(n-1)/2}(-1)^{\alpha}J_{2\beta+1}\left(k\left|\vec{\rho}_{n,\alpha}\right|\right)A_{n,\alpha}=-\frac{1}{4}\delta_{\beta,(n-1)/2},\ \beta=0,...,(n-1)/2 \tag{36}$$

and the remaining ones, express through them, through equalities

$$A_{n,n-\alpha}=A_{n,\alpha},\ \beta=0,...,(n-1)/2. \tag{37}$$

Similarly, for even n, the first $n/2$ unknowns can be determined from the system

$$\sum_{\alpha=0}^{(n/2)-1}(-1)^{\alpha}J_{2\beta}\left(k\left|\vec{\rho}_{n,\alpha}\right|\right)A_{n,\alpha}=\frac{1}{4}\delta_{\beta,n/2},\ \beta=1,...,n/2, \tag{38}$$

then determine the coefficient $A_{n,n/2}$ as

$$A_{n,n/2}=2\sum_{\alpha=0}^{(n/2)-1}(-1)^{\alpha+(n/2)-1}J_0\left(k\left|\vec{\rho}_{n,\alpha}\right|\right)A_{n,\alpha} \tag{39}$$

and the remaining $n/2$ unknowns, determine from the equalities

$$A_{n,n-\alpha}=A_{n,\alpha},\ \alpha=0,...,n/2-1. \tag{40}$$

The left parts of expressions (33) and (35) describe multipoles consisting of $n+1$ monopoles located, respectively, along the abscissa and ordinate axis, at points with radius vectors (29) and (34). Moreover, if the amplitudes $A_{n,\alpha}$ of these monopoles satisfy conditions (36), (37) or (38)-(40), depending on the parity of n, then their total fields coincide with the original fields (1) with sufficient accuracy. This type of multipole can be called linear.

The length of the considered multipole, for a given n, is determined as $l_n= nd_n$. Above we assumed that $kd_n=1/2$. If we reduce the value of kd_n (and therefore the length of the multipole), then the accuracy of expressions (33) and (35) will increase. It is interesting to compare the accuracy of the representation of fields (1) by a linear multipole and a circular multipole of the second type. Let us determine the radius ρ_0 of the circular multipole as $\rho_0=n/(4k)$. Then its diameter will be equal to the length of the linear multipole (Figure 7).

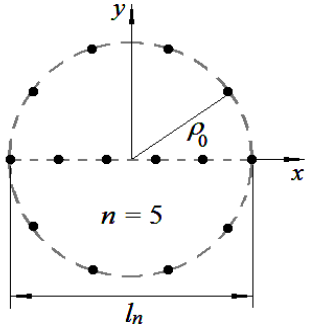

Figure 7. The second type of circular multipole and linear multipole

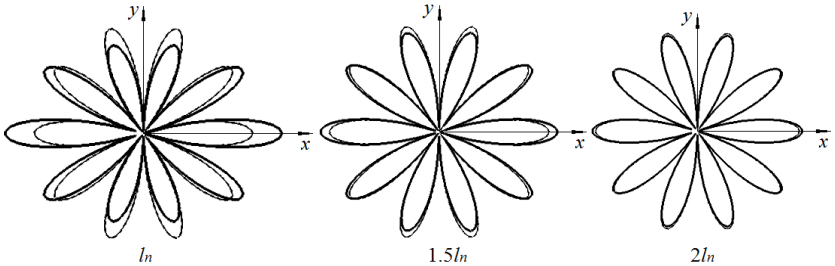

Figure 8. Comparison of amplitude radiation patterns of linear and circular multipoles

Figure 8 presents a comparison of the radiation patterns of the fields from the two types of multipoles under consideration, with the corresponding patterns of the field $H_n^{(1)}(k\rho)\cos(n\varphi)$, for n = 5. These radiation patterns are constructed at three different distances from the center of the multipoles (l_n, 1.5l_n and 2l_n). The patterns of linear and circular multipoles are marked with a thick and thin continuous line, respectively. The pattern of the field $H_n^{(1)}(k\rho)\cos(n\varphi)$ is marked with a dotted line. The thin continuous line is so close to the dashed line that at the given scales, they are indistinguishable. This demonstrates the high accuracy with which the second type circular multipoles describe fields (1). In contrast, the linear multipole exhibits comparatively lower accuracy, which, however, improves with increasing distance.

6. CONCLUSIONS

The structures of field sources described by wave functions (1) of a circular cylinder have been examined. By analyzing the radiation patterns of field (1) and applying the addition theorem for cylindrical functions, four types of multipoles have been identified. These vary in their structure, the number of monopoles, and the precision with which they represent the original fields. From the findings, it is concluded that a second type circular multipole, consisting of 2n monopoles, achieves higher accuracy. However, a smaller linear multipole, comprising n+1 monopoles, may offer greater optimality.

REFERENCES

[1] Stratton J., "Theory of Electromagnetism", Moscow, 1948.
[2] Darsavelidze I., "Multipole Representation of Certain Cylindrical WaveFunctions", XXVIII IEEE International Seminar/Workshop DIPED-2023, 97-101, 2023.
[3] Sobolev S. L., "Equations of mathematical physics", Moscow, 1966.
[4] Gradshtein I., Ryzhik I, "Tables of integrals, sums, series and products", Moscow, 1963.
[5] Bakhvalov N., Zhidkov N., Kobelkov G., "Numerical methods", Moscow, 2011.
[6] Fridman A. E., "Fundamentals of metrology". Modern course, St. Petersburg, 2008.
[7] Abramowitz M., Stegun I., "Handbook of mathematical functions with formulas, graphs and mathematical tables", US Department of commerce, 1972.

A SYSTEM FOR DIGITIZING ANALOG SIGNALS, COMPRESSION AND ENCRYPTION

Dilyana Dimitrova*

* Department of Information Technologies, Nikola Vaptsarov Naval Academy

73 Vasil Drumev Str., Varna, Bulgaria.

E-mail: di.dimitrova@naval-acad.bg

(Selected from CEMA'24 Conference)

Abstract

This paper investigates the digitization, compression and encryption of analog signals. Digitization transforms analog signals into discrete digital form, crucial for efficient data processing and transmission in diverse industries. A-law compression is used to optimize the dynamic range of the signals by reducing the data needed to represent them while maintaining acceptable quality. Results demonstrate analog-to-digital conversion of sinusoidal signal and voice using an 8-bit ADC, confirming minimal signal loss with higher quantization levels. AES encryption is used to secure the digitized and compressed signal, ensuring data privacy. Future research will explore signal recovery methods and automated encryption techniques using Simulink. This study underscores the importance of digitization and encryption technologies in advancing communication systems reliability and security.

Keywords: ADC, AES, cryptography, digitization, encryption, signals, voice.

1. INTRODUCTION

In today's rapidly evolving world, the digitization of signals and voice plays a central role in numerous aspects of our everyday life. Digitization refers to the process of converting analog signals, which are continuous and variable, into digital ones, which are discrete and binary. This transformation is crucial for many reasons, spanning from enhanced data processing capabilities to improved storage and transmission efficiency.

In an era where the Internet of Things (IoT) is becoming widespread, the seamless connectivity between smart devices, sensors, and control systems is made possible through digital communication. This connectivity enables real-time monitoring, data

analysis, and automation, driving efficiency and innovation across industries such as healthcare, transportation, and manufacturing.

Digital signals can be easily compressed, encrypted, and stored, offering significant advantages in terms of data management and security. Techniques like A-law compression, commonly used in Europe, allow efficient use of bandwidth and storage space. Encryption ensures that digital information can be transmitted securely, protecting sensitive data from unauthorized access and cyber threats.

In the field of voice communication, digitization has transformed how people interact and communicate. From mobile phones to VoIP (Voice over Internet Protocol) services, the conversion of voice to digital signal has enabled clearer, more reliable, and more adaptable communication methods. Features such as voicemail, and video calls have become standard, enhancing personal and professional communication.

Different studies have been made in this field. In paper [1] authors propose an encryption technology for voice transmission in mobile networks using the 3DES-ECC algorithm. It combines speech signal acquisition, 3DES, and ECC algorithms for speech data encryption. In [2] is presented speech to text conversion system that also encrypts the text using the Advanced Encryption Standard (AES) algorithm. In [3] authors introduce a k-shuffle based audio scrambling technique that produces cipher audio with variable audibility, beneficial for perceptual video encryption algorithms, showing resistance to certain types of attacks.

The absence of an analog-to-digital converter (ADC) that uses A-law compression and encryption of the signal following the literature review underscores the relevance of the issue.

The models in this paper present source digitization and A-law compression. A possibility for signal encryption is provided. For this purpose, two examples of digitization are examined – a sinusoidal signal, to clearly observe the signal transformation, and voice. The analog-to-digital converter is a fundamental block that enables the conversion of information from analog to digital form and its transmission to digital devices. Without analog-to-digital conversion, the world today would be very different. An A-law compression is selected because it is used in Europe.

The main aim of the paper is to explore and demonstrate the processes of analog-to-digital conversion and A-law compression in the context of digitizing signals, specifically sinusoidal signals and voice. Additionally, the paper highlights the significance of these processes in enhancing signal quality, reducing noise, and improving the efficiency of digital signal transmission. The study also investigates the application of encryption techniques, particularly using symmetric cryptographic algorithms like AES, to secure the digitized and compressed signals.

2. SOURCE DIGITIZATION

2.1. Components of the block diagram

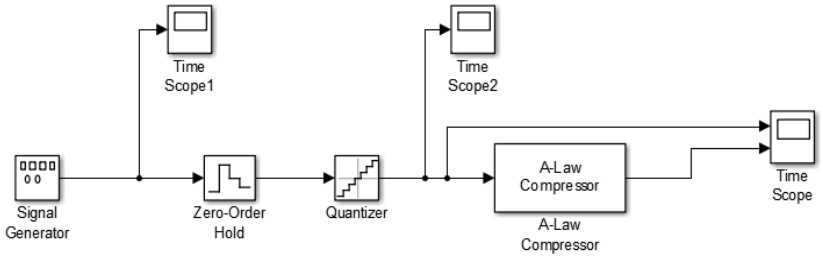

Figure 1. Block diagram of an ADC with A-law signal compression.

Figure 1 presents a block diagram of analog-to-digital conversion with A-law signal compression made in Simulink. The following blocks are used:

- Signal Generator - used to generate a sinusoidal signal.
- Zero-Order Hold - this block samples the signal at specific time intervals, Δt. According to the Kotelnikov-Nyquist theorem [4], if there is a signal with a frequency band from f_{min} to f_{max} and take the reciprocal of the doubled maximum value of the frequency band, the time interval Δt should be less than or equal to this value to transmit it accurately to the receiver without distortion. This can be presented with formula (1).

$$\Delta t \leq \frac{1}{2f_{max}} \tag{1}$$

- Quantizer - discretizes the signal by amplitude and rounds it to the nearest allowed level. Rounding to an integer leads to distortion of the original signal and errors at the receiving end. There is a quantization step between two allowed levels, which is uneven, and the quantization is even.

- A-law Compressor - it uses an algorithm to compresses the signal's dynamic range and improves its quality.
- Several oscilloscopes that visually display the analog-to-digital conversion process.

2.2. Results from the source digitization simulation

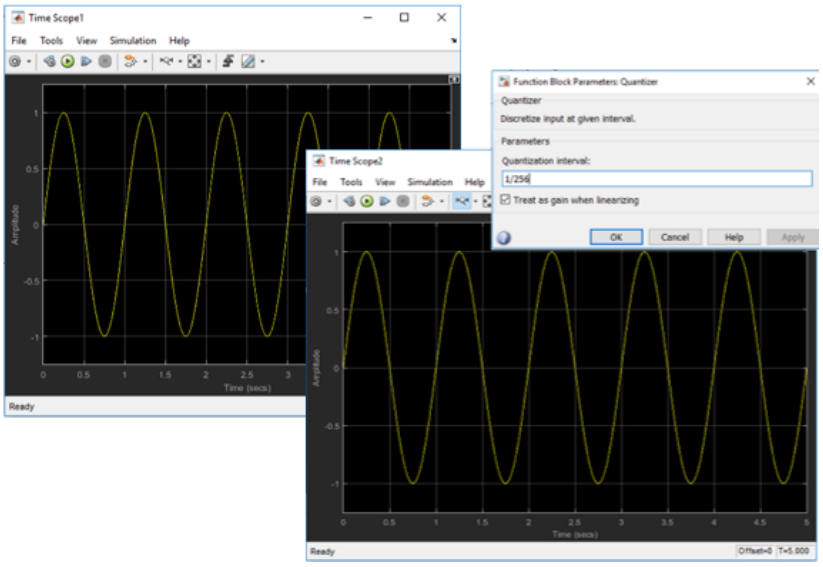

Figure 2. Graph of the analog signal from oscilloscope “Time Scope1” and the digital signal from “Time Scope2” with a quantization interval of 1/256.

According to ITU-T standard G.711 for pulse-code modulation (PCM) of speech frequencies [5], the best signal digitization is achieved using 256 quantization levels because it uses 8 bits for encoding speech. Therefore, the quantization interval in this case is equal to 1/256. After examining the oscilloscope graphs with this value, it was found that there is no visual difference between the analog and digital signals, as it is shown on Fig. 2, indicating that the conversion was performed with almost no loss.

To clearly observe the conversion of the analog signal to digital, and after testing different values that are powers of two, a noticeable difference in the graph without zooming in was seen at a quantization interval value of 1/32.

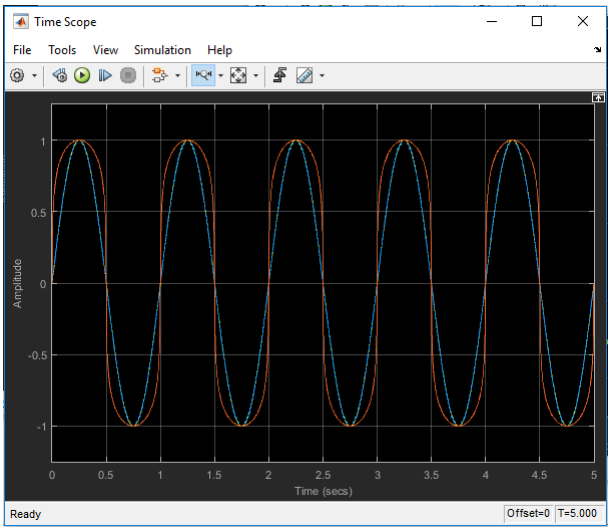

Figure 3. Graph from the "Time Scope" oscilloscope of the signal before and after analog-to-digital conversion and after A-law compression.

In Fig. 3, the analog signal and the digital signal are overlaid, and the A-law compressed signal, shown in red, clearly demonstrates that the quantization interval is non-uniform for the latter. The purpose of the compression is to improve the quality of the transmitted signal. In conclusion of the experiment, lower levels are more probable and carry more information, so they are quantized with a smaller step. The opposite is true for higher levels, so they are quantized with a larger step.

3. DIGITIZATION OF VOICE

3.1. Components of the block diagram

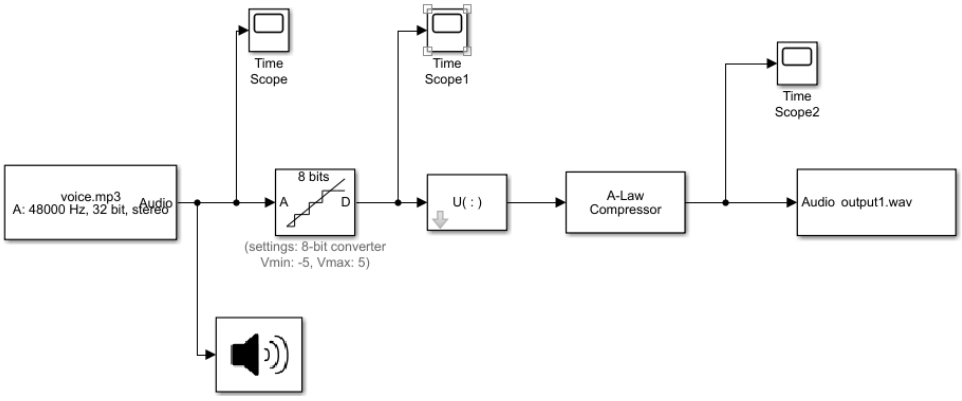

Figure 4. Block diagram of voice digitization.

In Fig. 4, a block diagram of voice digitization is presented. Its purpose is to demonstrate how speech is converted from analog to digital form and what happens to the signal after A-law compression. The following elements are used:

- Block that loads an audio file (From Multimedia file) - the file contains the author's voice in m4a format or MPEG audio encoding. The signal is dual-channel since it is stereo and is recorded using phone's built-in microphone.
- Analog-to-Digital Converter (Idealized ADC quantizer) - used to convert voice signals, as using individual components for analog-to-digital conversion from the first diagram significantly increases the simulation time. In accordance with ITU-T standard G.711 for pulse-code modulation (PCM) of speech frequencies [5], an 8-bit ADC is utilized.
- Block for converting 2-D signal to 1-D - converts the two-dimensional stereo signal into a one-dimensional format, as the A-law compression block requires a one-dimensional input signal.
- A-law Compressor - the same as the one in first experiment.
- "To Audio Device" block - used for playback of the audio file.
- Oscilloscopes - used for graphical visualization of analog-to-digital conversion and A-law compression.

3.2. Results from the voice digitization simulation

In Fig. 5, two graphs illustrate the digital signal of the voice after processing by the ADC and a magnified view of it. These clearly show the analog-to-digital conversion. The signal is in two colors because it is dual-channel.

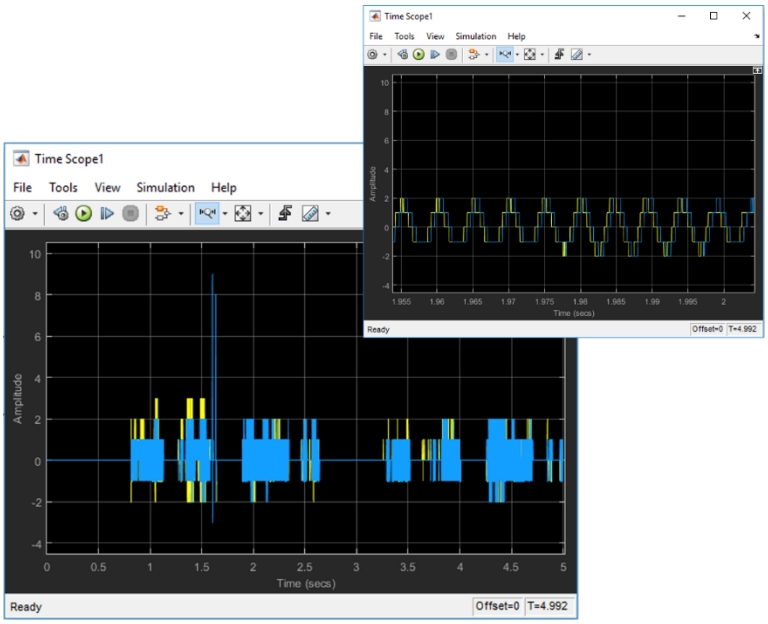

Figure 5. Graphs of the digitized signal (voice) from the "Time Scope1" oscilloscope.

Fig. 6 presents graphs of the signal after A-law compression. The wide dynamic range of speech is not well encoded by standard ADCs and their linear coding, as the quantization step is the same, leading to errors during analog signal reconstruction. For this purpose, A-law compression is used, where low frequencies are quantized with a smaller step and high frequencies - with a larger one, reducing the dynamic range of speech, minimizing quantization noise, and enhancing the quality of the transmitted digital signal.

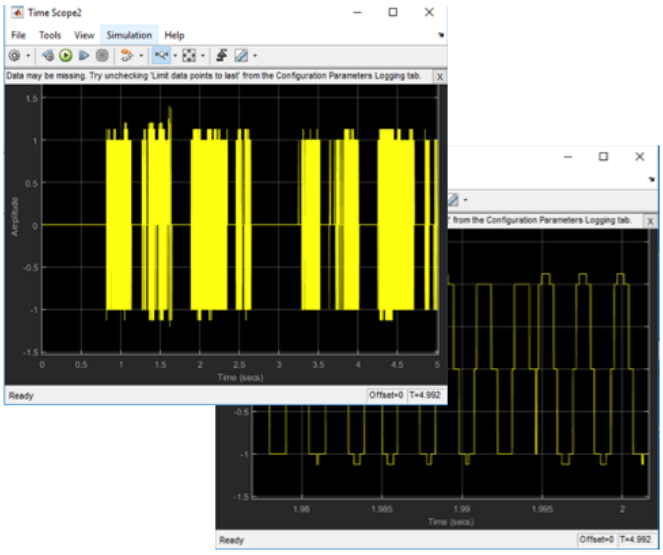

Figure 6. Graphs of the signal after A-law compression from "Time Scope2" oscilloscope.

4. ENCRYPTION

For encrypting the digitized and compressed signal, various cryptographic algorithms can be used. Symmetric cryptographic algorithms like AES are recommended for encryption of large volumes of information. During the experiment, AES encryption algorithm is utilized.

There are several approaches that can be implemented for encrypting the digitized and compressed signal. In this specific solution, the compressed signal is first saved into a WAV file using the built-in Simulink block "To Multimedia File". Subsequently, a MATLAB function is created to convert it into a binary file. The binary file is then encrypted with AES using external software. The decryption and information recovery processes were successful. As this paper is focused on digitizing the source signal, recovering the signal at the receiver will be a subject of future work.

Another potential approach for encrypting the digitized and compressed signal involves creating a Simulink function that automates the described procedures, which also remains a subject for future investigation.

5. CONCLUSION

During the study, graphical analog-to-digital conversion and A-law compression of sinusoidal signal and speech were observed. A possibility for signal encryption is provided. It was found that using higher levels of quantization provides better digitization of the analog signal. In the first case, 32 levels were used to observe the digitization process more closely. Comparing this with 256-level quantization, the digital signal showed no visible difference from the analog signal on the graph, indicating minimal loss during inverse conversion. In the second scheme, voice analog-to-digital conversion was performed using an 8-bit ADC according to G.711 standard, applying the same principles as in the first scheme. A-law compression was utilized in both cases to improve the quality of the transmitted digital signal. To secure the digitized and compressed signal, different cryptographic algorithms can be applied. Symmetric ciphers such as AES are preferred for their effectiveness with large data sets. In this experiment, AES was specifically utilized to encrypt the signal, providing strong security. Future research will explore signal recovery methods and automated encryption techniques using Simulink.

This study underscores the importance of digitization and encryption in advancing communication systems reliability and security.

The report is in implementation of the National Scientific Program "Security and Defense", adopted with RMS No. 731/21.10.2021, and financed by the Ministry of Education and Science of the Republic of Bulgaria according to Agreement No. D01-74/19.05.2022.

REFERENCES

[1] Chang, Z., Woźniak, M. Encryption technology of voice transmission in mobile network based on 3DES-ECC algorithm. Mobile Netw Appl 25, 2398–2408 (2020). https://doi.org/10.1007/s11036-020-01617-0

[2] Agarwal, A., Raj, P.M., & Katiyar, S. (2019). Secured Audio Encryption using AES Algorithm. International Journal of Computer Applications.

[3] Alhassan, S., Iddrisu, M.M. & Daabo, M.I. Securing audio data using K-shuffle technique. Multimed Tools Appl 78, 33985–33997 (2019). https://doi.org/10.1007/s11042-019-08151-6.

[4] V. V. Zamaruiev, "The use of Kotelnikov-Nyquist-Shannon sampling theorem for designing of digital control system for a power converter," 2017 IEEE First Ukraine Conference on Electrical and Computer Engineering (UKRCON), Kyiv, UKraine, 2017, pp. 522-527, doi: 10.1109/UKRCON.2017.8100305.

[5] International Telecommunication Union. "Recommendation G.711: Pulse Code Modulation (PCM) of Voice Frequencies." Accessed June 20, 2024. https://www.itu.int/rec/T-REC-G.711/.